Photonic–Plasmonic Mode Coupling in On-Chip Integrated Optoplasmonic Molecules

Wonmi Ahn, Svetlana V. Boriskina, Yan Hong, and Björn M. Reinhard*

Department of Chemistry and The Photonics Center, Boston University, Boston, Massachusetts 02215, United States

ABSTRACT We investigate photonic–plasmonic mode coupling in a new class of optoplasmonic materials that comprise dielectric microspheres and noble metal nanostructures in a morphologically well-defined on-chip platform. Discrete networks of optoplasmonic elements, referred to as optoplasmonic molecules, were generated through a combination of top-down fabrication and template-guided self-assembly. This approach facilitated a precise and controllable vertical and horizontal positioning of the plasmonic elements relative to the whispering gallery mode (WGM) microspheres. The plasmonic nanostructures were positioned in or close to the equatorial plane of the dielectric microspheres where the fields associated with the plasmonic modes can synergistically interact with the evanescent fields of the WGMs. We characterized the far-field scattering spectra of discrete optoplasmonic molecules that comprised two coupled 2.048 μm diameter polystyrene microspheres each encircled by four 148 nm diameter Au nanoparticles (NPs), through far-field scattering spectroscopy. We observed a broadening of the TE and TM modes in the scattering spectra of the optoplasmonic dimers indicative of an efficient photonic–plasmonic mode coupling between the coupled photonic modes of the WGM resonators and the localized surface plasmon modes of the NPs. Our experimental findings are supported by generalized multiple particle Mie theory simulations, which provide additional information about the spatial distributions of the near fields associated with the photonic–plasmonic hybrid modes in the investigated optoplasmonic molecules. The simulations reveal partial localization of the spectrally sharp hybrid modes outside of the WGM microspheres on the Au NPs where the local E-field intensity is enhanced by approximately 2 orders of magnitude over that of an individual Au NP.

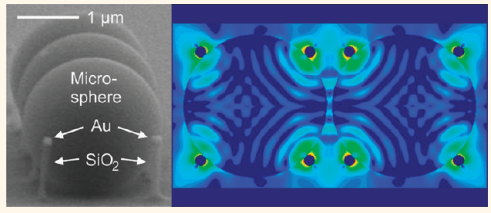

KEYWORDS: whispering gallery mode · integrated optical circuits · self-assembly · nanofabrication · photonic molecules · optical microcavity · plasmonics

Noble metal nanostructures sustain localized surface plasmons (LSPs), which—as coherent electron oscillations—provide the means for localizing incident electromagnetic radiation into nanoscale volumes.[1–5] The light focusing effect of nanoplasmonic structures and the ability to tune their near- and far-field responses simply by variation of their size and shape have triggered significant interest in nanoplasmonics for bridging the gap between photonics and electronics.[6,7] Indeed, the "plasmonic revolution" has already led to some exciting schemes for information and energy processing on nanometer length scales.[8–12] However, robust schemes for active nanoscale field modulation and spatial control, frequency switching, and reversible energy transfer between photons, surface plasmons, and nanoscale emitters are still largely missing in conventional nanoplasmonic circuitry due to fundamental limitations in the physical or chemical properties of the materials used to fabricate them. Theoretical work by us[13–16] and others[17–22] have shown that discrete optoplasmonic elements, which integrate high-*Q* optical microcavity (OM) resonators and plasmonic nanostructures into hybrid structures with well-defined geometric configurations, can address some of the limitations of current plasmonic nanocircuitry. We have recently proposed hybrid optoplasmonic structures (termed optoplasmonic superlenses) that combine the capability of OMs to insulate molecule–photon systems from decohering environmental effects with the superior light focusing properties of plasmonic nanoantennas.[13,14] Our theoretical analyses revealed that these optoplasmonic superlenses can achieve an efficient long-range transfer and subsequent refocusing of emitted photons into nanoscale volumes where they become accessible to near- and far-field detection. Enhanced information and energy transfer in optoplasmonic materials due to greatly reduced dissipative losses when compared to plasmonic waveguides is only one example where optoplasmonics creates new functionalities beyond the capabilities of the individual building blocks. We anticipate that optoplasmonic components will also facilitate active nanoplasmonic circuit elements for field modulation

* Address correspondence to bmr@bu.edu.

Received for review November 24, 2011 and accepted December 8, 2011.

Published online December 08, 2011
10.1021/nn204577v

and frequency switching,[14] as photon recycling in microcavities—in the form of high-*Q* whispering gallery modes (WGM)—translates into narrow linewidths and thus greatly enhances mode sensitivities to external stimuli and environmental changes.[23−25] OMs strongly modify radiative rates of quantum emitters at the WGM resonances by generating increased local density of states (LDOS).[26−29] The increase in LDOS together with the ability to shift WGM resonances through external stimuli could pave the way to dynamically reconfigurable optoplasmonic nanocircuits, enable the rational tuning of the absorption and emission rates of quantum emitters, and eventually lead to sensors with high sensitivity and high spectral resolution.[16,21]

Sensing applications, in particular, would benefit from the fact that the formation of hybrid photonic−plasmonic modes in optoplasmonic materials results in the redistribution of light between the plasmonic and photonic components. As a consequence, locations with high local E-field intensity are generated in the vicinity of the plasmonic components. These "hot-spots" lie outside of the OMs and are, thus, accessible to analytes in the environment.[13,16,21] Optoplasmonic structures offer, therefore, a viable strategy for overcoming the intrinsic limitation of OMs that their high-*Q* resonance modes are largely confined to their interior.

Previous experimental studies aimed at achieving synergistic photonic−plasmonic mode coupling in discrete optoplasmonic structures relied either on the direct attachment of noble metal nanoparticles (NPs) to large (hundreds of micrometers in diameter) microspheres[19,21,30,31] or on the manual contacting of surface-immobilized noble metal nanostructures through mechanically supported large microspheres.[16] These approaches, however, do not allow for a miniaturization and on-chip integration of optoplasmonic elements, leave little room for rational performance optimization, and cannot generate more complex optoplasmonic networks comprising multiple coupled WGMs. There is, consequently, a real need for rational fabrication approaches to explore and ultimately realize the full potential of optoplasmonics.

The greatest challenge for a successful on-chip integration of plasmonic and photonic elements is that the WGM field in surface-supported microsphere is concentrated in its equatorial plane located micrometers above the substrate, where it is difficult to access with standard fabrication approaches.[32,33] We address this challenge in this article by introducing a novel nanofabrication strategy for optoplasmonic structures that enables a precise and controllable vertical and horizontal positioning of plasmonic elements relative to the embedded microspheres and, thus, ensures that the WGM evanescent field and plasmonic antenna modes interact synergistically.

We applied this approach in this work to fabricate discrete optoplasmonic elements comprising 2.048 μm diameter polystyrene (PS) microspheres encircled in the equatorial plane by four 148 nm diameter Au NPs in a rectangular arrangement as well as linear networks of these optoplasmonic elements. In analogy to the concepts of photonic atoms[34] and molecules,[35−41] which describe individual OMs (photonic atoms) and coupled OMs (photonic molecules), we refer to optoplasmonic structures comprising one dielectric microsphere as optoplasmonic atoms and structures with multiple coupled dielectric microspheres as optoplasmonic molecules, in the following. The ability to assemble several photonic and plasmonic components into optoplasmonic molecules with defined morphology is a major strength of our fabrication approach since it paves the way to utilizing photonic, plasmonic, and photonic−plasmonic mode coupling between the building blocks to shape specific near- and far-field responses.

In this exploratory study we investigate the far-field spectral response of selected optoplasmonic molecules through polarization-resolved far-field scattering spectroscopy. Our experiments reveal a strong coupling between the photonic modes of the OMs and the LSPs of adjacent NPs in the fabricated optoplasmonic structures. These experimental results are in excellent agreement with state-of-the-art computational simulations that provide additional insight into the—as yet largely unknown—underlying physical mechanism governing the near- and far-field responses of these novel electromagnetic materials.

RESULTS AND DISCUSSION

Template-Assisted Self-Assembly of Optoplasmonic Atoms and Molecules. Figure 1 outlines the template-guided self-assembly approach we applied to fabricate optoplasmonic atoms and molecules that contain spherical Au NPs in the equatorial plane of microspheres. The basic idea of our fabrication approach is to generate spherical Au NPs on nanopillars of predefined height that create a "binding cavity" that is then filled with dielectric microspheres. The height (*h*) of the nanopillars (including the radius of the Au NPs) is chosen to correspond to the radius of the microspheres of interest, and in optoplasmonic molecules the separation between the nanopillars of two separate optoplasmonic atoms can be varied to tune the photonic mode coupling between the OMs in a rational fashion.[36,37,42,43] The microspheres are inserted into the created binding cavities by dewetting a solution of microspheres across the substrate.[44]

To achieve an efficient capture of microspheres, the binding cavities are created slightly larger than required by geometric considerations alone. For the 2.048 μm diameter polystyrene microspheres used in this work, we used binding cavities with a diameter of 2.100−2.200 μm. The microspheres caught in the cavities have, consequently, some play, and the separation between the microsphere surface and the Au NPs is subject to some variation. In the structures fabricated

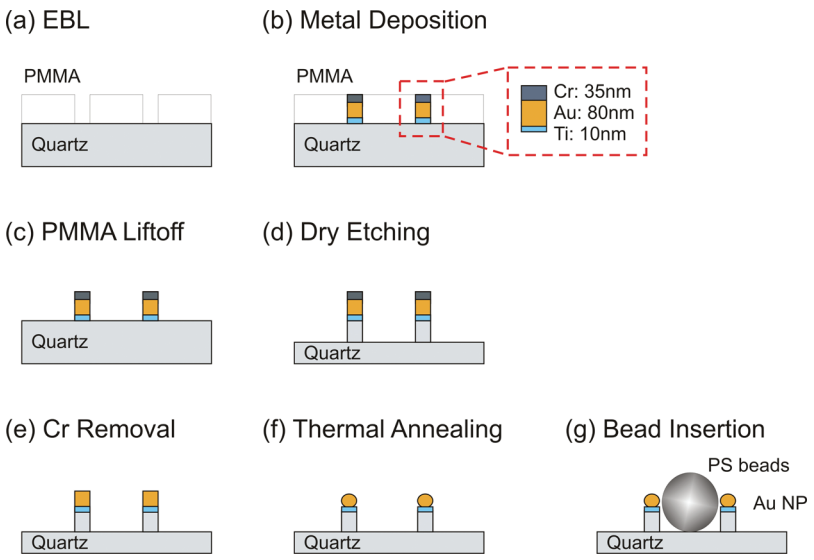

Figure 1. Schematic illustration of the fabrication process for hybrid optoplasmonic structures: (a) nanopatterning using electron-beam lithography (EBL), (b) metal deposition (Ti/Au/Cr = 10/80/35 nm), (c) lift-off of PMMA photoresist layer, (d) reactive ion etching (RIE) to create nanopillars by etching down the exposed (*i.e.*, not Cr covered) quartz substrate areas, (e) Cr layer removal, (f) thermal annealing to create spherical Au NPs, and (g) insertion of polystyrene microspheres into the pillar cavities *via* convective self-assembly to position Au NPs in the equatorial plane of the dielectric microsphere.

in this study the separation between the surfaces of the Au NPs and the dielectric microspheres varied between a few nm to tens of nm. According to generalized multiparticle Mie theory (GMT) simulations (Figure S1) the electromagnetic coupling between the WGM and the LSPs is very tolerant against fluctuations in the OM–Au NP separation; we observed a synergistic effect of the photonic–plasmonic mode coupling on the near-field intensity for separations at least up to 100 nm. The separations between the photonic and plasmonic components in the fabricated optoplasmonic structures are therefore sufficiently small to warrant strong electromagnetic interactions. We anticipate that an optimization of the assembly process will achieve an improvement of the fitting accuracy and result in an enhanced control of the Au NP–dielectric microsphere separation in the future.

Figure 2 shows scanning electron microscope (SEM) images of optoplasmonic structures that contain one (a, b), two (c, d), or three (e, f) 2.048 μm diameter microspheres. The edge-to-edge distance (d_p) between neighboring pillars in the optoplasmonic molecules (c–f) was chosen as $d_p = 330$ nm to enable strong electromagnetic coupling between the individual constituent optoplasmonic atoms. At $d_p = 330$ nm the embedded microspheres are nearly touching, ensuring an efficient coupling of the WGM modes in the dimer and trimer, respectively. The height of the pillars (h) in the structures was determined to be ~870 nm from SEM images acquired at a tilt angle of $\theta = 80°$ using the formula $h = h_m/\sin(\theta)$, where h_m is the measured length of pillars in the tilted SEM image. In the magnified view ($\theta = 70°$) of a representative nanopillar scaffold in Figure 2g the spherical Au NPs on top of the created nanopillars are clearly visible. The diameter of the Au NP in these optoplasmonic structures is 148 nm. Figure 2h confirms that the spherical Au NPs are located in the equatorial plane of the PS microspheres inserted into the binding cavities.

Far-Field Scattering Spectroscopy of Optoplasmonic Dimers and Their Photonic and Plasmonic Building Blocks. One experimental approach to detect photonic–plasmonic mode coupling in optoplasmonic molecules is to probe for changes in the far-field response of coupled OMs that occur in the presence of Au NPs. Scattering spectra of individual microsphere dimers with or without plasmonic nanostructures are conveniently recorded in a dark-field microscope under white-light illumination from a xenon lamp ($\lambda = 380–720$ nm) at oblique excitation angles as shown in Figure 3a (see Methods). Polarization-resolved far-field scattering spectra can be obtained in this setup by placing a polarizer in the beam path after the objective. The polarizer facilitates the acquisition of scattering spectra for light polarizations parallel or perpendicular to the long axis of the optoplasmonic molecules.

Our optoplasmonic structures contain three different building blocks: OMs, Au NPs, and SiO_2 nanopillars. Before we characterize the far-field spectra of discrete optoplasmonic molecules in detail, we first want to characterize the influence of the dielectric nanopillars on the spectral response of individual OMs. Figure 3b compares the experimental far-field scattering spectra of an individual OM on a planar quartz substrate (blue), of an individual OM integrated into a nanopillar-defined binding cavity without gold NP (red), and the GMT-simulated spectrum of a free-space OM (black, refractive index of PS $n_r = 1.59$). The experimental spectra

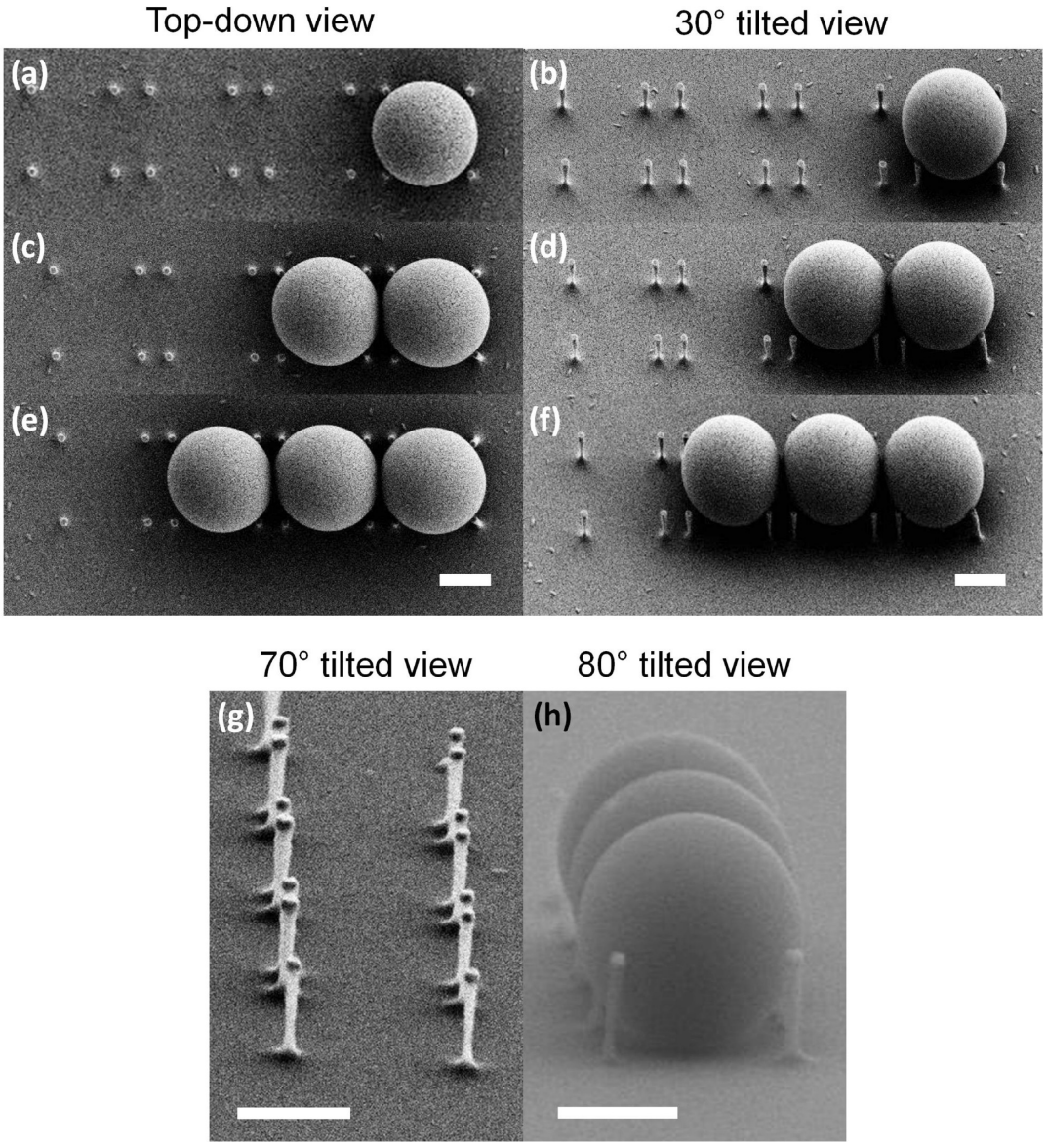

Figure 2. SEM images of optoplasmonic structures that contain one (a, b), two (c, d), or three (e, f) 2.048 μm diameter PS microspheres. The edge-to-edge distance between the pillars of two neighboring bindinig cavities is d_p = 330 nm, and the height of the pillars is h = 870 nm. The tilted SEM images (g, h) show that spherical Au NPs with a diameter of d = 148 nm are located in the equatorial plane of the PS microspheres trapped in the pillar cavities (scale bars = 1 μm).

with and without nanopillars (no gold tips) nearly superimpose, which clearly indicates that the effect of the nanopillars on the spectral response is small.

The simulation of the 2.048 μm diameter PS sphere in a homogeneous ambient medium with refractive index of n_r = 1 reproduces the experimental spectra overall very well. The spectra show a series of transverse electrical (TE) and transverse magnetic (TM) modes, which can be assigned through the simulations. Both TE and TM modes are classified by three indices: n, the radial order (the number of peaks in the intensity profile along the radial direction); m, the azimuthal mode index (the number of field variations along the sphere equator); and l, the number of waves in a cyclic orbit ($l - |m| + 1$ is equal to the number of peaks in the intensity profile of the mode along the meridian).[45,46] The most pronounced spectral peaks in Figure 3b correspond to the excitation of WG modes with n = 1 and $m = l$, which are indexed as TE(M)$_{m,1}$ modes. Figure 3c shows the E-field intensity distributions of the TE$_{15,1}$ and TM$_{14,1}$ WG modes in the PS microsphere under the excitation by an incident linearly polarized plane wave.

Figure 3d gives a systematic overview of the fitted WGM peak wavelength (λ_{peak}) and full width at half-maximum (fwhm) for the assigned modes in the microsphere (blue) and the nanopillar-embedded microsphere (red). The plots reveal that the nanopillars induce a slight blue-shift (~0.80 nm) and an almost negligible difference in the peak broadening (~0.37 nm). The most significant difference between the experimental

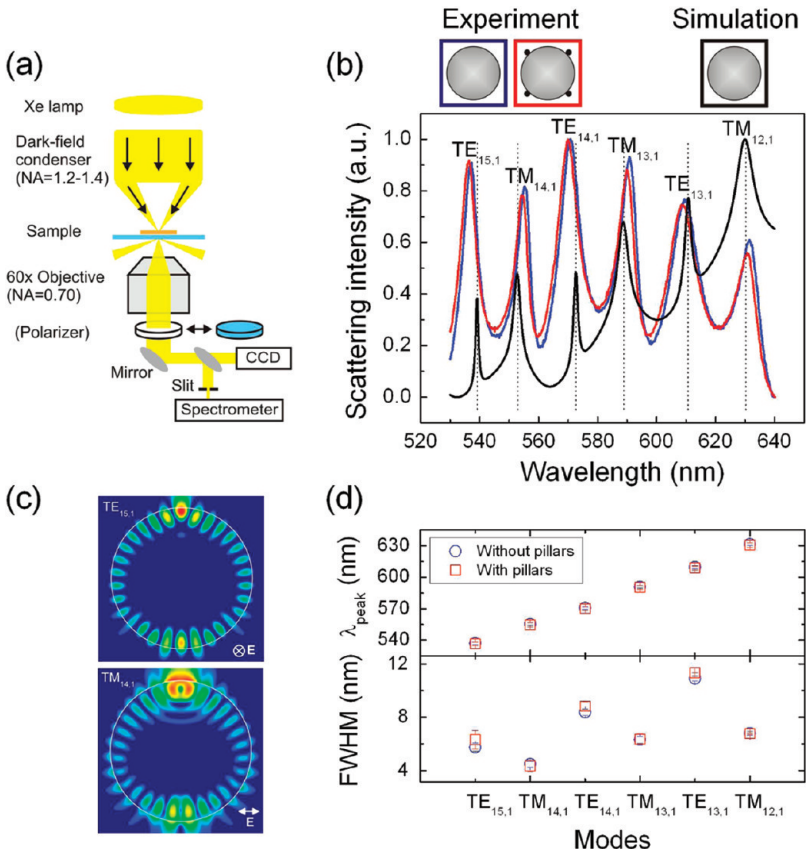

Figure 3. Far-field scattering spectroscopy of individual optical microcavities (OMs). (a) Dark-field spectroscopy setup used in our experiment. (b) Experimental far-field scattering spectra of an individual OM on a planar quartz substrate (blue) and of an individual OM integrated into a nanopillar-defined binding cavity missing gold NPs (red). The generalized multiple particle Mie theory (GMT) simulated OM spectrum (black) was obtained assuming an ambient refractive index of $n_r = 1$. Insets: Structures of the corresponding optoplasmonic atoms. (c) E-field intensity distributions of the $TE_{15,1}$ and $TM_{14,1}$ WGMs in the PS microsphere under excitation through an incident linearly polarized plane wave. (d) Experimental peak wavelength (λ_{peak}) and fwhm for individual WGMs.

and simulated spectra is that the experimental TE modes are broader than the TM modes, whereas the simulations predict the opposite trend. This finding indicates an additional loss channel in the experiments that is specific for the TE modes. A similar effect has been observed before by Mitsui *et al.*[33] in near-field scanning optical microscopy (NSOM) measurements of substrate-supported fluorescent PS beads. Analogous to the NSOM studies of Mitsui *et al.*, our scattering measurments predominantly detect horizontally polarized light emitted by TE and TM modes in two orthogonal planes. While the TM modes are circulating in the horizontal plane parallel to the surface of the SiO_2 substrate, the TE modes are confined to the vertical plane. Consequently, only the TE modes interact closely with the SiO_2 substrate along their path around the PS sphere. The resulting losses decrease the *Q* factor of the TE modes and account for the resulting spectral broadening.

After validating that the effect of the dielectric nanopillars does not significantly perturb the spectral response of the OMs, we want to analyze the scattering spectra of discrete optoplasmonic molecules for indications of photonic−plasmonic mode coupling in the next step. Since we are interested in the fundamental electromagnetic mechanisms governing the optical response of optoplasmonic molecules, we focus in this study on the simplest possible optoplasmonic molecule, the dimer. Figure 4a shows both the scattering image and the spectrally resolved scattering image of the equatorial plane of an optoplasmonic dimer recorded under unpolarized white-light excitation. We used the software of the electron multiplying charged coupled device (EMCCD) detector to confine the region of interest for the spectra acquisition to the highlighted area (dotted red box) in the center of the structure where the best signal-to-noise is obtained and where the coupling of the photonic modes of the two OMs is expected to be strongest.

The top panel in Figure 4b shows representative normalized scattering spectra of an optoplasmonic dimer (red) that consists of OM, Au NPs, and the SiO_2 nanopillars, and of a "photonic" dimer (blue) with an identical structure but without Au NPs on the nanopillars. The bottom panel in Figure 4b contains the GMT-simulated scattering spectra of the optoplasmonic dimer (red) and of the photonic dimer (blue) in an ambient medium of

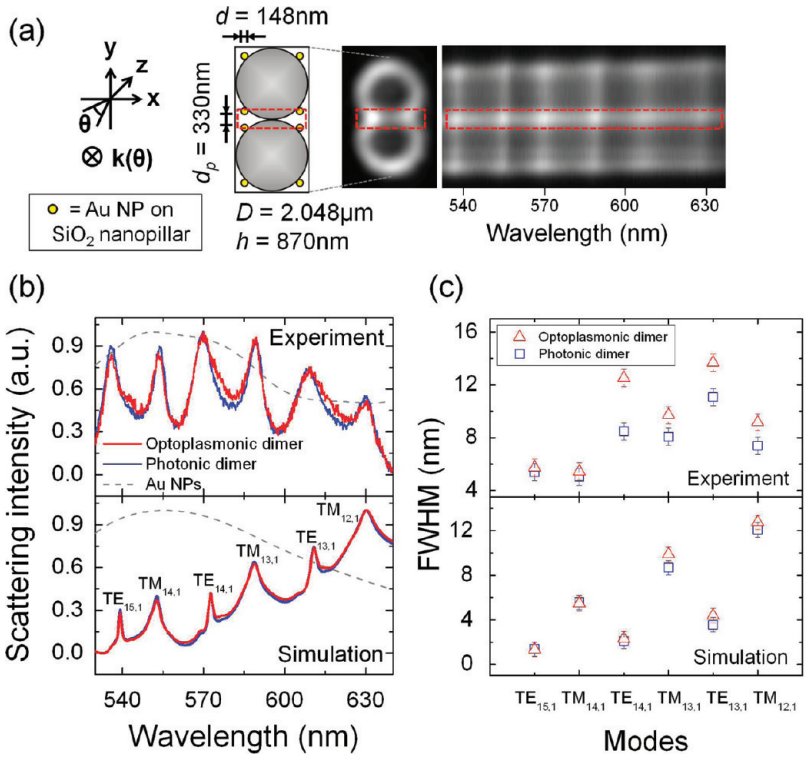

Figure 4. Far-field scattering spectroscopy of optoplasmonic and photonic dimers. (a) Geometric parameters, scattering image, and spectrally resolved scattering image of an optoplasmonic dimer recorded under unpolarized white-light excitation. Photonic dimers have the same geometry as the optoplasmonic dimers but lack Au NPs on the nanopillars. (b) Top panel: Experimental scattering spectra of the optoplasmonic (red) and the corresponding photonic dimer (blue). Bottom panel: GMT-simulated spectra of the optoplasmonic (red) and photonic dimer (blue). The scattering spectra of Au NPs obtained for the same geometry (d = 148 nm, d_p = 330 nm) but without nanopillars and microspheres are included as dashed gray lines. (c) fwhm of individual WGMs shown in (b).

refractive index $n_r = 1$ (for details pertaining to the simulations, please refer to the Methods section). The simulated spectra are in good agreement with the experimental spectra and enable an assignment of the spectral features in the dimer spectra. Both the experimental and theoretical spectra in Figure 4b indicate a measurable broadening of the spectral features in the optoplasmonic structure. The spectral broadening becomes more obvious in Figure 4c, where we plot the fwhm of the fitted peaks for the individual modes. For the lower m values investigated in this work the optoplasmonic TE and TM modes are broadened relative to their counterparts in the photonic dimers. Although the relative spectral broadening is more pronounced in the experiments than in the simulations, the latter reproduce the general trend well. For the same reasons discussed in Figure 3d for the optoplasmonic atoms, we find again that the TE modes are broader than the TM modes in the experimental spectra, although the simulations predict the opposite behavior.

We experimentally verified the TE and TM mode assignment in the optoplasmonic dimer through polarization-resolved scattering spectroscopy in Figure 5. This approach utilizes differences in the orientation of the horizontal E-field components of TE and TM modes in the equatorial plane of a microsphere relative to its surface.[47] In the junction of the two OMs, the TE mode is dominant for a light polarization perpendicular to the long dimer axis (Figure 5a), whereas the TM mode is observed for a light polarization parallel to the long dimer axis (Figure 5b). Here again, we observed the broadening of the individual modes (Figure S2) in the optoplasmonic dimer (red) relative to the photonic dimer (blue) as described above. The relative intensities of the individual peaks for the orthogonal light polarizations are consistent with their mode assignment obtained through comparison with theory (Figure S3).

The spectral broadening of the TE and TM modes observed in the optoplasmonic dimer in both theory and experiment is a direct consequence of photonic–plasmonic mode coupling, which is associated with a redistribution of light from the OMs into the NPs. Dissipative losses in the Au NPs shorten the lifetime of the hybridized modes and account for the observed broadening of the spectral features. In the optoplasmonic dimer every OM is located in the effective field of four NPs. Although this significant association of the OMs with Au NPs leads to a measurable peak broadening, the induced broadening is relatively small, which reaffirms the advantage of our experimental strategy to place Au NPs into the evanescent field of OMs in a controlled fashion.

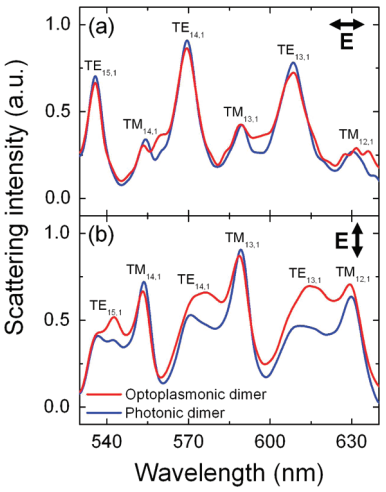

Figure 5. Polarization-resolved far-field scattering spectroscopy of optoplasmonic (red) and photonic (blue) dimers. Experimental spectra were acquired for the light polarization perpendicular to the dimer axis (a; TE mode dominant) and parallel to the dimer axis (b; TM mode dominant).

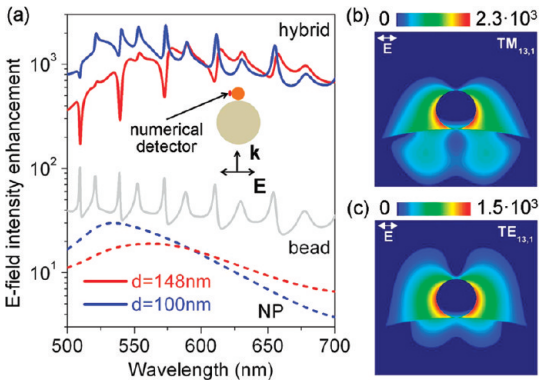

Figure 6. (a) E-field intensity enhancement in the hot-spot of a discrete optoplasmonic atom composed of a 2.048 μm polystyrene microsphere and an Au NP coupled *via* 1 nm air gap as a function of wavelength and NP diameter (red: d = 148 nm, blue: d = 100 nm). The spectra of an isolated microsphere (solid gray) and isolated Au NPs (dashed red: d = 148 nm, dashed blue: d = 100 nm) are shown for comparison. The inset shows a schematic of the optoplasmonic atom as well as the propagation and polarization direction of the illuminating plane wave. The position of the numerical detector for evaluating the E-field intensity enhancement spectra is indicated by a red dot. (b, c) Near-field intensity distributions on the Au NP (d = 148 nm) at the wavelengths of the hybrid photonic−plasmonic resonances corresponding to the excitation of $TM_{13,1}$ (b, λ = 589.7 nm) and $TE_{13,1}$ (c, λ = 614.4 nm) WGMs in the microsphere.

Figure 4b contains the scattering spectra of the Au NPs used in this work as dashed gray lines. The 148 nm diameter spheres have a broad resonance that peaks at ~555 nm in both the experimental and simulated spectra. The photonic−plasmonic resonances in the optoplasmonic dimer are dramatically sharper than those of the Au NPs, and our simulations (Figure S1) indicate that the resonant peaks remain sharp even in the case when NPs are almost in direct contact with the microsphere surface. The relative sharpness of the resonances in optoplasmonic dimers could translate into performance advantages over conventional plasmonic nanostructures, provided that a significant E-field localization outside of the OMs is achieved. The performed far-field scattering spectroscopy provides, however, no direct information about the E-field intensity spectrum or its spatial distribution in the fabricated optoplasmonic dimers. Instead, we will systematically characterize the near-field response of the fabricated optoplasmonic dimers using computational electromagnetics.

Electromagnetic Simulation of the Near Field in Optoplasmonic Dimers. Our combined experimental/theoretical characterization of the far-field scattering spectra has shown that GMT accurately reproduces the optical properties of the investigated optoplasmonic dimers. We, therefore, chose this already calibrated approach for investigating the near-field properties of the optoplasmonic dimers. To estimate the maximum electric field intensity that can be generated in the hot spots of the optoplasmonic molecules used in the experiments, we first plot the intensity enhancement on the surface of a microsphere-coupled NP for two different NP diameter in Figure 6. The structure is illuminated by a linearly polarized plane wave, and the field intensity is evaluated in the NP equator. Our simulations indicate that the most efficient coupling between photonic and plasmonic modes is achieved under illumination along the microsphere - Au NP axis. In this case, the E-field intensity on the NP surface can be increased by 2 orders of magnitude over that of an isolated NP (Figure 6a). By comparing these spectra with those of the isolated OM and of the isolated NPs, we conclude that the sharp spectral features in the spectra of the optoplasmonic structures originate from the coupling of the NP LSPs to the WGMs in the microsphere, while the overall shape of the spectra is determined by the broad NP LSP resonances. Figure 6a also shows that efficient LSP-WGM coupling preserves the spectral peaks of the WGMs and, at the same time, results in high resonant E-field enhancement on the NP occurs at frequencies corresponding to the longer wavelength tail of the LSP resonance. In contrast, WGM peaks with frequencies around or above the LSP resonance peak are strongly distorted due to the coupling to the NP. These effects are observed for both NP diameters. Figure 6b,c shows typical E-field intensity distributions around a hot-spot of a microsphere-coupled NP at selected TE and TM hybrid mode wavelengths. The plots show strong E-field intensity outside of the OM.

The assembly of OMs into photonic molecules of various configurations facilitates a coupling-induced tailoring of their far- and near-field spectra.[35−37,42] Optoplasmonic molecules offer now additional degrees of engineerability since photonic−photonic and photonic−plasmonic mode coupling can be combined. To demonstrate that efficient photonic−plasmonic coupling can be achieved in more complex optoplasmonic molecules, in Figure 7 we plot typical

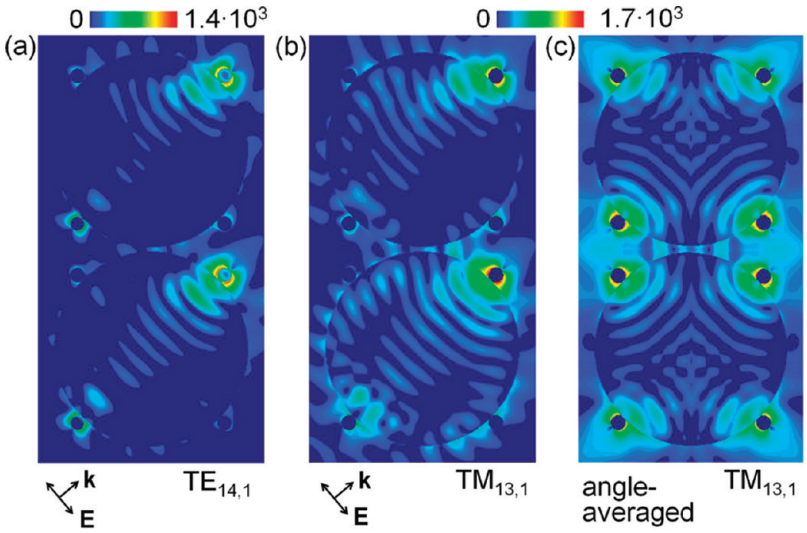

Figure 7. E-field intensity distributions in the optoplasmonic dimer at the wavelength of the hybrid $TE_{14,1}$ (a, λ = 580.9 nm) and $TM_{13,1}$ (b, λ = 590 nm) mode. The dimer is composed of two 2.048 μm microspheres, each encircled by four 148 nm diameter Au NPs separated from the microsphere surface by 1 nm gaps. The insets show the direction and polarization of the incident plane wave. (c) Near-field intensity distribution at the $TM_{13,1}$ mode wavelength averaged over the in-plane angle of incidence.

near-field distributions in the experimentally characterized optoplasmonic dimer for one selected angle of plane wave incidence (Figure 7a,b) and averaged over various incident angles (Figure 7c). Spatially selective intensity enhancement comparable with that in the simpler structure in Figure 6 is also observed for the optoplasmonic dimer. Most importantly, the electromagnetic hot-spots generated on the Au NPs are significantly enhanced over those on isolated NPs and are accessible to analytes and other nano-objects in their environment. The E-field enhancement at specific wavelengths generated by the optoplasmonic dimer can be used to enhance the sensitivities of refractometric-,[16,21] Raman-,[31] and fluorescence[13]-based sensors. Finally, the sensitivity of the E-field intensity patterns within the optoplasmonic dimer to the polarization of the incident light provides a mechanism for the wavelength- and polarization-selective spatial manipulation of nanoscale optical fields.

CONCLUSIONS

We combined plasmonic nanostructures and multiple dielectric OMs into discrete optoplasmonic molecules through accurate integration of PS microspheres into binding cavities formed by Au NP-tipped SiO_2 nanopillars *via* a convective self-assembly. We demonstrate that this approach facilitates an efficient realization of optoplasmonic molecules with well-defined geometries in an on-chip format. The high structural precision provided by the fabrication approach facilitates a rational control over the electromagnetic interactions between the plasmonic and photonic building blocks. Furthermore, the fabrication approach offers high design flexibility, as it is generally applicable to dielectric microspheres that can be synthesized from different materials with narrow size distributions. The refractive index of commercially available dielectric beads ranges from 1.47 (silica beads), to 1.59 (polystyrene beads), to 2.40 (carboxylated titania beads), and microspheres can be further doped selectively with fluorescent molecules or quantum dots.[38,39] We restricted our exploratory studies of the electromagnetic coupling mechanisms governing the optical properties of optoplasmonic molecules to the simplest optoplasmonic molecule, the dimer. Our combined experimental and theoretical studies of optoplasmonic dimers assembled from 2.048 μm diameter PS microspheres and 148 nm Au NPs in the equatorial plane of the OMs provide direct evidence for efficient photonic–plasmonic mode coupling in the optoplasmonic dimer. Our studies reveal partial mode localization of the hybrid modes on the Au NPs, where they are accessible to interact with the environment. The optoplasmonic molecules introduced in this work pave the way to more complex, on-chip integrated optoplasmonic networks that can overcome some of the intrinsic disadvantages associated with dissipative losses in Au NPs and that provide new opportunities for biosensing and for information and energy transfer and processing.

METHODS

Fabrication of Optoplasmonic Atoms and Molecules. In the first step, regular arrays of nanoholes of ~150 nm diameter were patterned in 200 nm thick PMMA layers spin-coated on a quartz substrate through electron beam lithography (EBL) using a Zeiss SUPRA 40VP scanning electron microscope equipped with a Raith Beam

Blanker and nanometer pattern generation system. A Ti/Au/Cr layer with a thickness of 10/80/35 nm, respectively, was then deposited on the EBL-patterned surface by electron beam evaporation (CHA Industries, Fermont, CA, USA) with deposition rates of 0.5/1.0/0.5 Å/s for each metal to create optoplasmonic dimers that consist of Au NPs. For photonic dimers that lack Au NPs on top of nanopillars, only a Cr layer was deposited on the substrate surface. A Ti layer improved adhesion of Au films to a quartz substrate, and a Cr layer protected the Au films from anisotropic dry etch gases. After the PMMA layer was lifted off by immersion in acetone for 1 min followed by 10, 20, and 30 s of sonication each in a fresh acetone bath, substrates were ready for reactive ion etching (RIE, Plasma-Therm. model 790). We used a mixture of CHF_3/O_2 (50/5 sccm, standard cubic centimeters per minute) at a pressure of 200 mTorr and a power of 150 W for a total etching time of 18−20 min. The anisotropic etching process removed the SiO_2 only in exposed areas, which were not protected by Cr layers, resulting in the formation of nanopillar arrays with Cr layer tips. The height of the nanopillars can be controlled through the RIE process parameters, including the etching time, power, pressure, and ratio between the two mixed gases. A RIE chamber was circulated with O_2 for 15 min and prerun with CHF_3/O_2 for 30 min prior to each RIE process on samples to ensure reproducible etching results. A Cr layer was removed by gentle swirling in a 40 °C Cr etchant solution for 15 s, and the substrate was rinsed with distilled water thoroughly. The substrate was then heated in a rapid thermal annealer (Molecular Process Technology Corp.) to 800 °C (3 min) to create *spherical* Au NPs on top of the nanopillars.

The regular arrays of micropillar cavities with defined widths and depths were then used as templates for the assembly of optoplasmonic structures. The created cavities were filled with PS microspheres using a convective self-assembly strategy. An aqueous solution of PS microspheres (2.048 μm in diameter; 1%; 50 μL) was sandwiched between the patterned microcavity substrate and a blank quartz substrate separated by a 380 μm gap. Upon evaporation of the water, the meniscus of the microsphere-containing solution was dragged across the substrate surface by capillary forces. These forces have a component perpendicular to the patterned surface,[44] which enabled an efficient trapping of microspheres in the cavities formed by the fabricated pillars. The insertion of microspheres into the Au NP-functionalized pillars completed the assembly of the optoplasmonic structures.

Polarization-Resolved Dark-Field Scattering Spectroscopy. Dark-field (DF) scattering spectra of the prepared optoplasmonic structures were recorded using an inverted microscope (Olympus IX71) equipped with an imaging spectroscopy detector (Andor Shamrock with Andor Newton EMCCD) as shown in Figure 3a. The samples were illuminated at oblique angles from the substrate side using an oil-immersion DF condenser (Olympus U-DCW, NA = 1.2−1.4). A xenon lamp (λ = 380−720 nm, Agilent Polychrome 3000) was used as illumination source. The light scattered from the sample was collected with a 60× air objective lens (Olympus LUCPLFLN, NA = 0.7), and a polarizer (Olympus U-POT) was placed after the objective to record polarization-resolved scattering spectra.

Spectrum Processing. The spectral images taken using exposure times of 0.3 s (20 accumulations) were background corrected by subtraction of spectral signals taken from an equally sized, unpatterned adjacent area. The scattering spectra were additionally corrected by the excitation profile of the white-light source by normalizing with the scattering spectrum of a white-light scatterer on a piranha-etched quartz substrate. To calculate the fwhm of individual WGM peaks, the scattering spectra were fit to Lorentzian peak functions using OriginPro (v.8.5.0, SR1, OriginLab Corp.).

Computational Electromagnetics. Both, far- and near-field spectra of optoplasmonic molecules are calculated in the frame of the generalized multiparticle Mie theory, which provides an exact analytical solution of Maxwell's equations for an arbitrary configuration of L spheres.[48−50] The total electromagnetic field scattered by the multisphere structure is constructed as a superposition of partial fields scattered by each sphere: $\mathbf{E}^l_{sc} = \Sigma_{(n)}\Sigma_{(m)}(a^l_{mn}\mathbf{N}_{mn} + b^l_{mn}\mathbf{M}_{mn})$, $l = 1, ..., L$. A matrix equation for the Lorenz−Mie multipole scattering coefficients (a^l_{mn}, b^l_{mn}) is obtained by imposing the continuity conditions for the tangential components of the electric and magnetic fields on the particles' surfaces and by truncating the infinite series expansions to a maximum multipolar order N.

The scattering and absorption efficiencies are calculated as the normalized to unity scattering and absorption cross sections of a nanostructure under plane-wave illumination. To reproduce the experimental dark-field scattering spectra of optoplasmonic molecules under unpolarized white-light excitation, the spectra are calculated for the plane wave incidence at 55° to normal to the surface (to simulate oblique illumination) and averaged over the polar angle and polarization direction. The photonic dimer is simulated as a dimer of 2.048 μm diameter PS microspheres. In the optoplasmonic dimers each microsphere contains a set of four 148 nm diameter Au NPs in the equatorial plane (see schematic in Figure 4a). The exact geometric parameters reproduce the experimental values as determined by SEM. We used the experimentally obtained refractive index values from Johnson and Christy[51] for Au in the simulations.

Acknowledgment. This work was supported by the National Science Foundation through grants CBET-0853798 and CBET-0953121.

Supporting Information Available: Figures S1−S3. This material is available free of charge *via* the Internet at http://pubs.acs.org.

REFERENCES AND NOTES

1. Kreibig, U.; Vollmer, M. *Optical Properties of Metal Clusters*; Springer: Berlin, 1995.
2. Schuller, J. A.; Barnard, E. S.; Cai, W.; Jun, Y. C.; White, J. S.; Brongersma, M. L. Plasmonics for Extreme Light Concentration and Manipulation. *Nat. Mater.* **2010**, *9*, 193–204.
3. Halas, N. J.; Lal, S.; Chang, W.-S.; Link, S.; Nordlander, P. Plasmons in Strongly Coupled Metallic Nanostructures. *Chem. Rev.* **2011**, *111*, 3913–3961.
4. Giannini, V.; Fernández-Domínguez, A. I.; Sonnefraud, Y.; Roschuk, T.; Fernández-García, R.; Maier, S. A. Controlling Light Localization and Light−Matter Interactions with Nanoplasmonics. *Small* **2011**, *6*, 2498–2507.
5. Yan, B.; Boriskina, S. V.; Reinhard, B. M. Theory, Fabrication, and Applications of Nanoparticle Cluster Arrays in Plasmon Enhanced Biosensing. *J. Phys. Chem. C* **2011**, ASAP article, DOI: 10.1021/jp207821t.
6. Halas, N. J. Connecting the Dots: Reinventing Optics for Nanoscale Dimensions. *Proc. Natl. Acad. Sci. U. S. A.* **2009**, *106*, 3643–3644.
7. Alu, A.; Engheta, N. All Optical Metamaterial Circuit Board at the Nanoscale. *Phys. Rev. Lett.* **2009**, *103*, 143902.
8. Maier, S. A.; Kik, P. G.; Atwater, H. A.; Meltzer, S.; Harel, E.; Koel, B. E.; Requicha, A. A. G. Local Detection of Electromagnetic Energy Transport below the Diffraction Limit in Metal Nanoparticle Plasmon Waveguides. *Nat. Mater.* **2003**, *2*, 229–232.
9. Akimov, A. V.; Mukherjee, A.; Yu, C. L.; Chang, D. E.; Zibrov, A. S.; Hemmer, P. R.; Park, H.; Lukin, M. D. Generation of Single Optical Plasmons in Metallic Nanowires Coupled to Quantum Dots. *Nature* **2007**, *450*, 402–406.
10. Lal, S.; Link, S.; Halas, N. J. Nano-Optics from Sensing to Waveguiding. *Nat. Photonics* **2007**, *1*, 641–648.
11. Volkov, V. S.; Bozhevolnyi, S. I.; Devaux, E.; Laluet, J.-Y.; Ebbesen, T. W. Wavelength Selective Nanophotonic Components Utilizing Channel Plasmon Polaritons. *Nano Lett.* **2007**, *7*, 880–884.
12. Fang, Y.; Li, Z.; Huang, Y.; Zhang, S.; Nordlander, P.; Halas, N. J.; Xu, H. Branched Silver Nanowires as Controllable Plasmon Routers. *Nano Lett.* **2010**, *10*, 1950–1954.
13. Boriskina, S. V.; Reinhard, B. M. Spectrally and Spatially Configurable Superlenses for Optoplasmonic Nanocircuits. *Proc. Natl. Acad. Sci. U. S. A.* **2011**, *108*, 3147–3151.
14. Boriskina, S. V.; Reinhard, B. M. Adaptive On-Chip Control of Nano-Optical Fields with Optoplasmonic Vortex Nanogates. *Opt. Express* **2011**, *19*, 22305–22315.

15. Boriskina, S. V.; Reinhard, B. M. Molding the Flow of Light on the Nanoscale: From Vortex Nanogears to Phase-Operated Plasmonic Machinery. *Nanoscale* **2012**, *4*, 76−90.
16. Santiago-Cordoba, M. A.; Boriskina, S. V.; Vollmer, F.; Demirel, M. C. Nanoparticle-Based Protein Detection by Optical Shift of a Resonant Microcavity. *Appl. Phys. Lett.* **2011**, *99*, 073701.
17. Zou, S.; Schatz, G. C. Combining Micron-Size Glass Spheres with Silver Nanoparticles to Produce Extraordinary Field Enhancements for Surface-Enhanced Raman Scattering Applications. *Isr. J. Chem.* **2006**, *46*, 293–297.
18. Hattori, H. T.; Li, Z.; Liu, D.; Rukhlenko, I. D.; Premaratne, M. Coupling of Light from Microdisk Lasers into Plasmonic Nano-Antennas. *Opt. Express* **2009**, *17*, 20878–20884.
19. Melnikau, D.; Savateeva, D.; Chuvilin, A.; Hillenbrand, R.; Rakovich, Y. P. Whispering Gallery Mode Resonators with J-Aggregates. *Opt. Express* **2011**, *19*, 22280–22291.
20. Chamanzar, M.; Adibi, A. Hybrid Nanoplasmonic-Photonic Resonators for Efficient Coupling of Light to Single Plasmonic Nanoresonators. *Opt. Express* **2011**, *19*, 22292–22304.
21. Shopova, S. I.; Rajmangal, R.; Holler, S.; Arnold, S. Plasmonic Enhancement of a Whispering-Gallery-Mode Biosensor for Single Nanoparticle Detection. *Appl. Phys. Lett.* **2011**, *98*, 243104–3.
22. Devilez, A.; Stout, B.; Bonod, N. Compact Metallo-Dielectric Optical Antenna for Ultra Directional and Enhanced Radiative Emission. *ACS Nano* **2010**, *4*, 3390–3396.
23. Emelett, S. J.; Soref, R. Design and Simulation of Silicon Microring Optical Routing Switches. *J. Lightwave Technol.* **2005**, *23*, 1800.
24. Almeida, V. R.; Barrios, C. A.; Panepucci, R. R.; Lipson, M. All-Optical Control of Light on a Silicon Chip. *Nature* **2004**, *431*, 1081–1084.
25. Djordjev, K.; Seung-June, C.; Sang-Jun, C.; Dapkus, R. D. Microdisk Tunable Resonant Filters and Switches. *IEEE Photon. Technol. Lett.* **2002**, *14*, 828–830.
26. Vernooy, D. W.; Furusawa, A.; Georgiades, N. P.; Ilchenko, V. S.; Kimble, H. J. Cavity QED with High-Q Whispering Gallery Modes. *Phys. Rev. A* **1998**, *57*, R2293.
27. Badolato, A.; Hennessy, K.; Atature, M.; Dreiser, J.; Hu, E.; Petroff, P. M.; Imamoglu, A. Deterministic Coupling of Single Quantum Dots to Single Nanocavity Modes. *Science* **2005**, *308*, 1158–1161.
28. Folan, L. M.; Arnold, S.; Druger, S. D. Enhanced Energy Transfer within a Microparticle. *Chem. Phys. Lett.* **1985**, *118*, 322–327.
29. Gotzinger, S.; de S. Menezes, L.; Mazzei, A.; Kuhn, S.; Sandoghdar, V.; Benson, O. Controlled Photon Transfer between Two Individual Nanoemitters *via* Shared High-Q Modes of a Microsphere Resonator. *Nano Lett.* **2006**, *6*, 1151–1154.
30. Shopova, S.; Blackledge, C.; Rosenberger, A. Enhanced Evanescent Coupling to Whispering-Gallery Modes Due to Gold Nanorods Grown on the Microresonator Surface. *Appl. Phys. B: Laser Opt.* **2008**, *93*, 183–187.
31. White, I.; Oveys, H.; Fan, X. Increasing the Enhancement of SERS with Dielectric Microsphere Resonators. *Spectroscopy* **2006**, *21*, 36.
32. Astratov, V. N.; Franchak, J. P.; Ashili, S. P. Optical Coupling and Transport Phenomena in Chains of Spherical Dielectric Microresonators with Size Disorder. *Appl. Phys. Lett.* **2004**, *85*, 5508–5510.
33. Mitsui, T.; Wakayama, Y.; Onodera, T.; Takaya, Y.; Oikawa, H. Observation of Light Propagation Across a 90° Corner in Chains of Microspheres on a Patterned Substrate. *Opt. Lett.* **2008**, *33*, 1189–1191.
34. Arnold, S. Microspheres, Photonic Atoms and the Physics of Nothing. *Am. Sci.* **2001**, *89*, 414–421.
35. Boriskina, S. V.; Chremmos, I.; Schwelb, O.; Uzunoglu, N., Eds. Photonic Molecules and Spectral Engineering. In *Photonic Microresonator Research and Applications*; Springer: Berlin/Heidelberg: 2010; Vol. 156, pp 393−421.
36. Boriskina, S. V. Theoretical Prediction of a Dramatic Q-Factor Enhancement and Degeneracy Removal of Whispering Gallery Modes in Symmetrical Photonic Molecules. *Opt. Lett.* **2006**, *31*, 338–340.
37. Boriskina, S. V. Coupling of Whispering-Gallery Modes in Size-Mismatched Microdisk Photonic Molecules. *Opt. Lett.* **2007**, *32*, 1557–1559.
38. Moller, B. M.; Woggon, U.; Artemyev, M. V.; Wannemacher, R. Photonic Molecules Doped with Semiconductor Nanocrystals. *Phys. Rev. B* **2004**, *70*, 115323–5.
39. Rakovich, Y. P.; Gerlach, M.; Bradley, A. L.; Donegan, J. F.; Connolly, T. M.; Boland, J. J.; Przyjalgowski, M. A.; Ryder, A.; Gaponik, N.; Rogach, A. L. Confined Optical Modes in Small Photonic Molecules with Semiconductor Nanocrystals. *J. Appl. Phys.* **2004**, *96*, 6761–6765.
40. Hara, Y.; Mukaiyama, T.; Takeda, K.; Kuwata-Gonokami, M. Photonic Molecule Lasing. *Opt. Lett.* **2003**, *28*, 2437–2439.
41. Bayer, M.; Gutbrod, T.; Reithmaier, J. P.; Forchel, A.; Reinecke, T. L.; Knipp, P. A.; Dremin, A. A.; Kulakovskii, V. D. Optical Modes in Photonic Molecules. *Phys. Rev. Lett.* **1998**, *81*, 2582.
42. Boriskina, S. V. Spectrally Engineered Photonic Molecules As Optical Sensors with Enhanced Sensitivity: A Proposal and Numerical Analysis. *J. Opt. Soc. Am. B* **2006**, *23*, 1565–1573.
43. Smotrova, E. I.; Nosich, A. I.; Benson, T. M.; Sewell, P. Optical Coupling of Whispering-Gallery Modes of Two Identical Microdisks and Its Effect on Photonic Molecule Lasing. *IEEE J. Select. Top. Quantum Electron* **2006**, *12*, 78–85.
44. Xia, Y.; Yin, Y.; Lu, Y.; McLellan, J. Template-Assisted Self-Assembly of Spherical Colloids into Complex and Controllable Structures. *Adv. Funct. Mater.* **2003**, *13*, 907–918.
45. Johnson, B. R. Theory of Morphology-Dependent Resonances: Shape Resonances and Width Formulas. *J. Opt. Soc. Am. A* **1993**, *10*, 343–352.
46. Teraoka, I.; Arnold, S. Resonance Shifts of Counterpropagating Whispering-Gallery Modes: Degenerate Perturbation Theory and Application to Resonator Sensors with Axial Symmetry. *J. Opt. Soc. Am. B* **2009**, *26*, 1321–1329.
47. Moller, B.; Woggon, U.; Artemyev, M. V. Photons in Coupled Microsphere Resonators. *J. Opt. A* **2006**, *8*, S113–S121.
48. Mackowski, D. W. Calculation of Total Cross Sections of Multiple-Sphere Clusters. *J. Opt. Soc. Am. A* **1994**, *11*, 2851–2861.
49. Xu, Y.-l. Electromagnetic Scattering by an Aggregate of Spheres. *Appl. Opt.* **1995**, *34*, 4573–4588.
50. Gopinath, A.; Boriskina, S. V.; Feng, N.-N.; Reinhard, B. M.; Negro, L. D. Photonic-Plasmonic Scattering Resonances in Deterministic Aperiodic Structures. *Nano Lett.* **2008**, *8*, 2423–2431.
51. Johnson, P. B.; Christy, R. W. Optical Constants of the Noble Metals. *Phys. Rev. B* **1972**, *6*, 4370.